Role of the entrance channel in the production of complex fragments in fusion-fission and quasifission reactions in the framework of the dinuclear system model

Sh. A. Kalandarov,[1,2] G. G. Adamian,[1,2] N. V. Antonenko,[1] W. Scheid,[3] and J. P. Wieleczko[4]
[1]*Joint Institute for Nuclear Research, 141980 Dubna, Russia*
[2]*Institute of Nuclear Physics, 702132 Tashkent, Uzbekistan*
[3]*Institut für Theoretische Physik der Justus–Liebig–Universität, D-35392 Giessen, Germany*
[4]*Grand Accélérateur National d'Ions Lourds (GANIL), F-14076 Caen, France*
(Received 3 August 2011; revised manuscript received 12 October 2011; published 2 December 2011)

The influence of entrance channel isospin, charge asymmetry, and bombarding energy on the competition between the complete fusion followed by the decay of compound nucleus and quasifission channels is treated within the dinuclear system model. The charge (mass) distributions of the products in the reactions ^{16,22}O+^{27}Al, ^{92,78}Kr+^{40}Ca, ^{86}Kr+^{48}Ca, ^{122}Sn+^{12}C, ^{32}S+^{100}Mo, ^{48}Ca+^{144,154}Sm, and ^{20,28}Ne+^{181}Ta are calculated at bombarding energies above the Coulomb barrier. The evolution of charge distribution of the complex fragments from the excited rotating nucleus ^{134}Xe with increasing angular momentum and excitation energy is demonstrated.

DOI: 10.1103/PhysRevC.84.064601 PACS number(s): 25.70.Gh, 24.10.Pa, 24.60.Dr

I. INTRODUCTION

The entrance channel isospin, charge asymmetry, and bombarding energy play an important role in the quasifission process, emission of the complex fragments ($Z > 3$), and formation of a compound nucleus (CN) and in the competition of decay channels in the excited CN [1]. The probability of the complex fragment emission as a function of these variables deserves study because of the increasing interest in the production of exotic nuclei via cluster decay of the CN [2–6].

There are different models [7–14] for describing the complex fragment emission. The code GEMINI [14] treats the sequential statistical evaporation and binary decay of a hot CN and makes a sharp distinction between the decay widths for emission of light particles and those for emission of complex fragments. The widths for emission of light particles are calculated using the Hauser-Feshbach approach with sharp cutoff transmission coefficients. The complex fragment emission width is treated within the generalized transition state concept proposed in Ref. [15]. The rotating finite-range model [16] or the rotating liquid-drop model is used to calculate the conditional barriers for binary division. The mass asymmetric fission barriers extracted from the experimental excitation functions lie between the values calculated with these two models [17,18]. Applications of the statistical model [14] are restricted to CN formation and for a good description of the charge (mass) distribution the maximum angular momentum J_{max} of the system is specially adjusted.

The main objective of the present work is to study the influence of the entrance channel isospin, charge asymmetry, and deposited energy on the charge distribution of the reaction products. The detailed theoretical study of the reactions ^{92,78}Kr+^{40}Ca, ^{86}Kr+^{48}Ca, ^{122}Sn+^{12}C, and ^{32}S+^{100}Mo at low bombarding energies will be carried out within the dinuclear system (DNS) model [19,20]. In this model the cluster emission is treated under the assumption that the light clusters are produced by a collective motion of the nuclear system in the charge asymmetry coordinate with further thermal escape over the Coulomb barrier. The emission barriers for complex fragments are calculated within the DNS model by using the double-folding procedure (with the Skyrme-type density-depending effective nucleon-nucleon interaction) for the nuclear part of the nucleus-nucleus interaction potential. Both the evaporation and binary decay are treated in the same way. The correct definition of the emission barriers and of their dependence on the angular momentum allows us to calculate the charge, mass, and kinetic energy distributions of the emitted complex fragments. The main ingredient of our description is the sophisticated potential energy as a function of angular momentum. The difference with respect to the statistical model [14] is a more accurate definition of the emission barriers. In our case J_{max} is not an adjustable parameter and is calculated within our model by using the nucleus-nucleus interaction potential [19,20]. In the reactions treated, the dynamics plays a role at high angular momenta when the quasifission becomes important. This clearly influences on the yields of fission-like fragments. Note that the high angular momenta J have larger contribution to the cross section. To test the model description, the calculated results were successfully compared with available experimental data for the reactions ^{3}He+^{nat}Ag, ^{78,86}Kr+^{12}C, ^{63}Cu+^{12}C, ^{93}Nb+^{9}Be,^{12}C, ^{45}Sc+^{65}Cu, ^{84}Kr+^{27}Al, ^{86}Kr+^{63}Cu, ^{4}He+^{130}Te, ^{40}Ca+^{78,82}Kr, and ^{139}La+^{12}C,^{27}Al at low bombarding energies [6,19,20].

It should be stressed that the present model is mainly limited by the low incident energies. Processes such as fast multifragmentation and nonequilibrium phenomena [21,22] are presently out of the scope of the DNS model. The transport Boltzmann-Uehling-Uhlenbeck-like models [21] can be used to describe fast fragment production, nonequilibrium phenomena, and the competition between fusion-fission and quasifission, similar to the DNS model. Being microscopic, transport models are more ambitious than macroscopic models. Since the microscopic effective interaction is an input there, they allow us to address fundamental questions on the interaction such as the density dependence of the symmetry

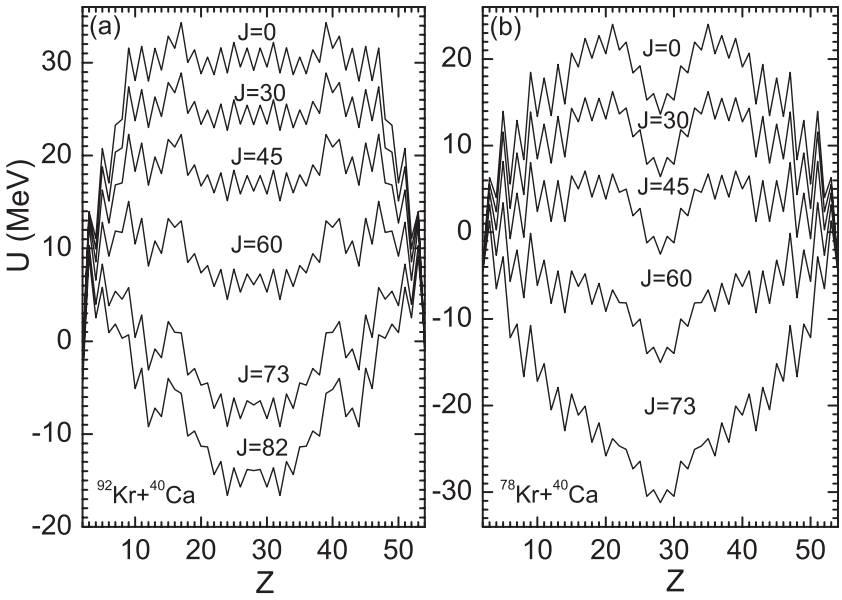

FIG. 1. Driving potentials at different angular momenta J for the systems (a) ^{92}Kr+^{40}Ca and (b) ^{78}Kr+^{40}Ca. The value of U is normalized to the energy of the rotating CN. The value of A is related to Z to supply the minimum of U.

energy, which is not possible within a macroscopic approach. Conversely, a macroscopic approach by definition uses more phenomenological inputs which are directly fixed on nuclear data; therefore its predictive power is higher. Moreover, it can combine reaction mechanism information with structure properties: a nice example is the observable staggering, which is completely inaccessible to the transport calculations [21], which have no pairing. For example, the DNS model contains the pairing energy and shell corrections through the experimental binding energies of the DNS nuclei.

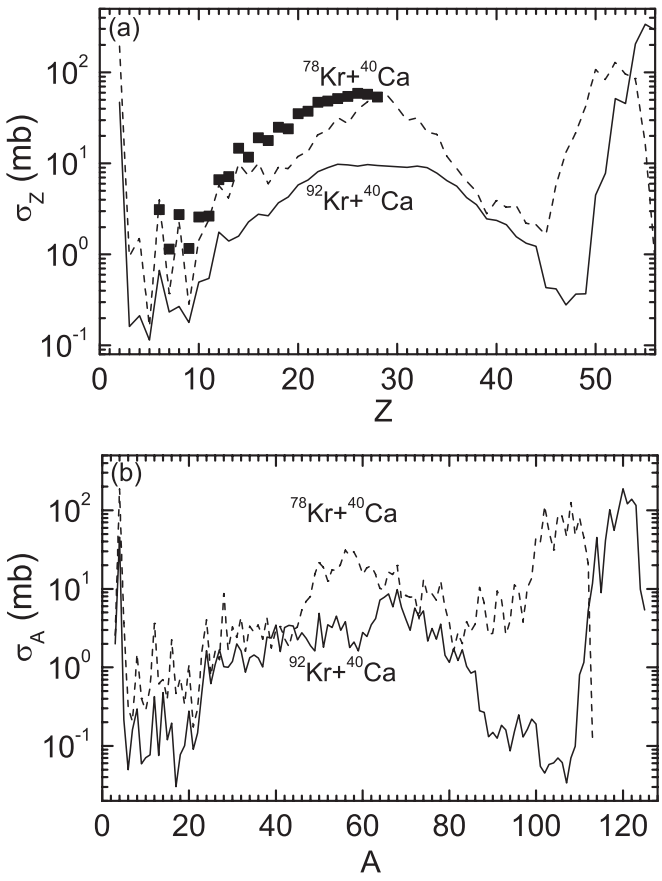

FIG. 2. Calculated charge (upper part) and mass (lower part) distributions of the products in the reactions ^{78}Kr+^{40}Ca (dashed line) and ^{92}Kr+^{40}Ca (solid line) at bombarding energy $E_{\rm lab}$ = 5.5 MeV/nucleon. The experimental data [6] for the ^{78}Kr+^{40}Ca reaction are shown by the squares.

II. MODEL

The DNS model [19,20,23] describes an evolution of the charge and mass asymmetry degrees of freedom, which are defined here by the charge and mass (neutron) numbers Z and A ($N = A - Z$) of light nucleus of the DNS, in the DNS formed in the entrance channel of the reaction after

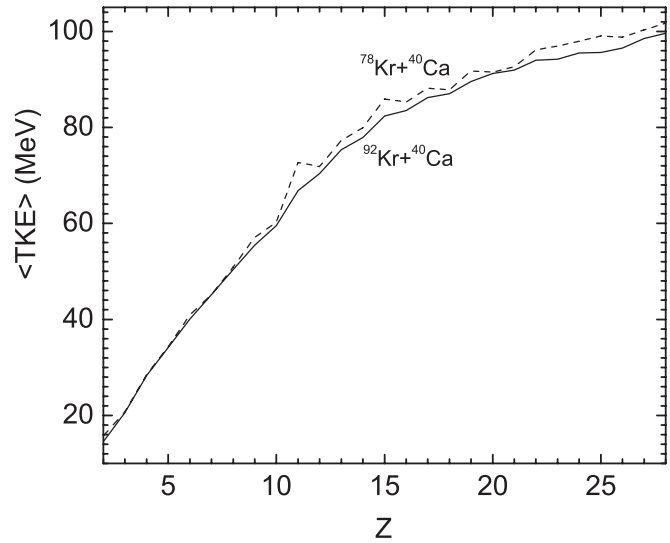

FIG. 3. Calculated average TKE of the products in the reactions ^{78}Kr+^{40}Ca (dashed line) and ^{92}Kr+^{40}Ca (solid line) at bombarding energy $E_{\rm lab}$ = 5.5 MeV/nucleon.

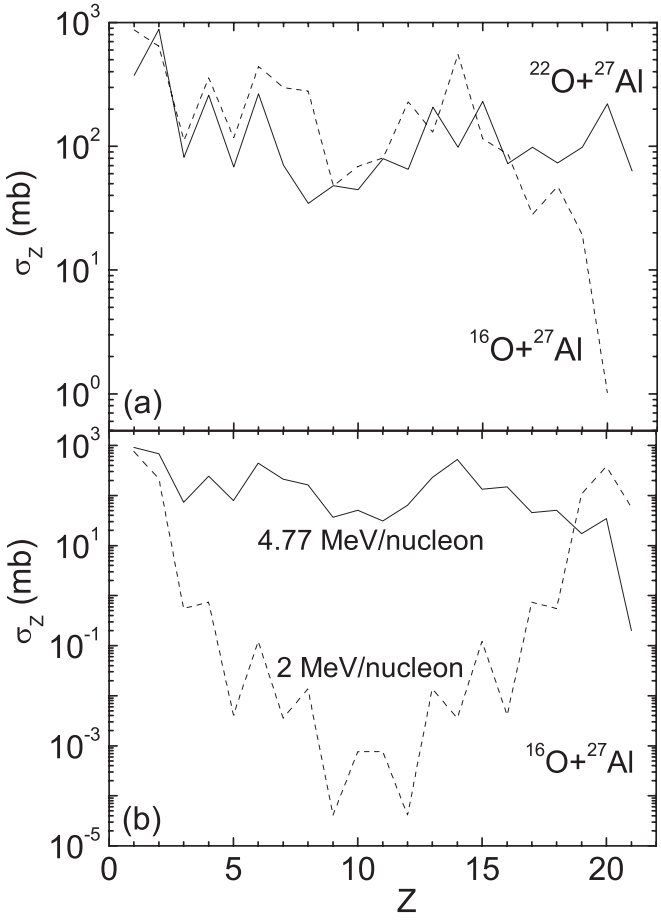

FIG. 4. (a) Calculated charge distributions of the products in the reactions ^{16}O+^{27}Al (dashed line) and ^{22}O+^{27}Al (solid line) at $E_{\rm lab}$ = 5.9 MeV/nucleon and 2.95 MeV/nucleon, respectively. (b) Calculated charge distributions of the products in the reaction ^{16}O+^{27}Al at $E_{\rm lab}$ = 2 MeV/nucleon (dashed line) and 4.77 MeV/nucleon (solid line).

the dissipation of the kinetic energy and angular momentum of relative motion. According to this description, there are nucleon drift and nucleon diffusion between the DNS nuclei and eventually either the CN is formed (the complete fusion) or the DNS with given Z and A is formed and decays (quasifission). After the formation, the excited CN decays by various channels including the formation of certain dinuclear systems and their decay. The CN formation and its consequent decay are not necessarily the ultimate results of the evolution of the initial DNS. In addition to contributions from the CN decay, the binary decay component is related to the quasifission mechanism. The competition between the complete fusion and quasifission depends on the value of the maximum angular momentum deposited in the system. The quasifission and CN decays are hardly distinguished in the experiments because in both cases two fragments are produced by the decay of the DNS formed during the diffusion process in the mass (charge) asymmetry coordinate with and without the CN formation stage.

The production cross section of a nucleus with charge Z and mass A numbers is calculated as follows [19]:

$$\sigma_{Z,A}(E_{\rm c.m.}) = \sum_{J=0}^{J_{\rm max}} \sigma_{Z,A}(E_{\rm c.m.}, J) = \sum_{J=0}^{J_{\rm max}} \sigma_{\rm cap}(E_{\rm c.m.}, J) W_{Z,A}(E^*_{\rm CN}, J), \quad (1)$$

where $\sigma_{\rm cap}$ is the partial capture cross section, which defines the transition of the colliding nuclei over the Coulomb barrier and the formation of the initial DNS when the kinetic energy $E_{\rm c.m.}$ and angular momentum J of the relative motion are transformed into the excitation energy and angular momentum of the DNS. This transition probability is calculated with the Hill-Wheeler formula. The value of $W_{Z,A}(E^*_{\rm CN}, J)$ is the formation-decay probability of the DNS with given asymmetries Z and A. The probability of the DNS formation is calculated statistically by using the stationary solution of the master equation with respect to the charge and mass asymmetries and depends on the potential energy of the DNS configurations at touching distance and on the thermodynamical temperature. The probability of the DNS decay in relative distance R is calculated by using the transition state method. This probability depends on the difference between the potential energies of the DNS configurations at the touching distance and at the barrier position. The maximum value of angular momentum $J_{\rm max}$ is limited by either the kinematical angular momentum $J_{\rm kin} = \{2\mu[E_{\rm c.m.} - V(R_b)]/\hbar^2\}^{1/2} R_b$ [where R_b is the position of the Coulomb barrier with the height $V(R_b)$ and μ is the reduced mass] or by the calculated critical angular momentum J_{cr}, depending on which one is smaller: $J_{\rm max} = \min[J_{\rm kin}, J_{cr}]$. It should be noted that the calculated capture cross sections with this method are in good agreement with those obtained with the dynamical model [24]. The details of calculations of $\sigma_{\rm cap}$, $W_{Z,A}(E^*_{\rm CN}, J)$, and, correspondingly, $\sigma_{Z,A}(E_{\rm c.m.})$ are given in Ref. [19]. Here, only the most salient features are outlined.

The DNS is trapped in the pocket of the interaction potential between partners. Then, a statistical equilibrium is reached in the mass-asymmetry coordinate so that the formation probability $P_{Z,A}$ of each DNS or CN configuration depends on the potential energy

$$U(R_m, Z, A, J) = B_1 + B_2 + V(R_m, Z, A, J) - \left[B_{12} + E^{\rm rot}_{12}(J)\right],$$

calculated with respect to the potential energy $B_{12} + E^{\rm rot}_{12}(J)$ [where B_{12} is the mass excess of the CN and the rotational energy $E^{\rm rot}_{12}(J)$ of the CN] of the rotational CN, where R_m is the location of the minimum of the pocket in the nucleus-nucleus interaction potential V and B_1 and B_2 are the mass excesses of fragments in their ground states. After the capture stage, there are nucleon drift and nucleon diffusion between the nuclei which constitute the DNS. Then, the excited DNS can decay with a probability $P^R_{Z,A}$ in the R coordinate if the local excitation energy of the DNS is high enough to overcome the barrier in the nucleus-nucleus potential. Ultimately, the system evolves either toward a CN configuration that subsequently decays or to a DNS configuration. The latter process, in which

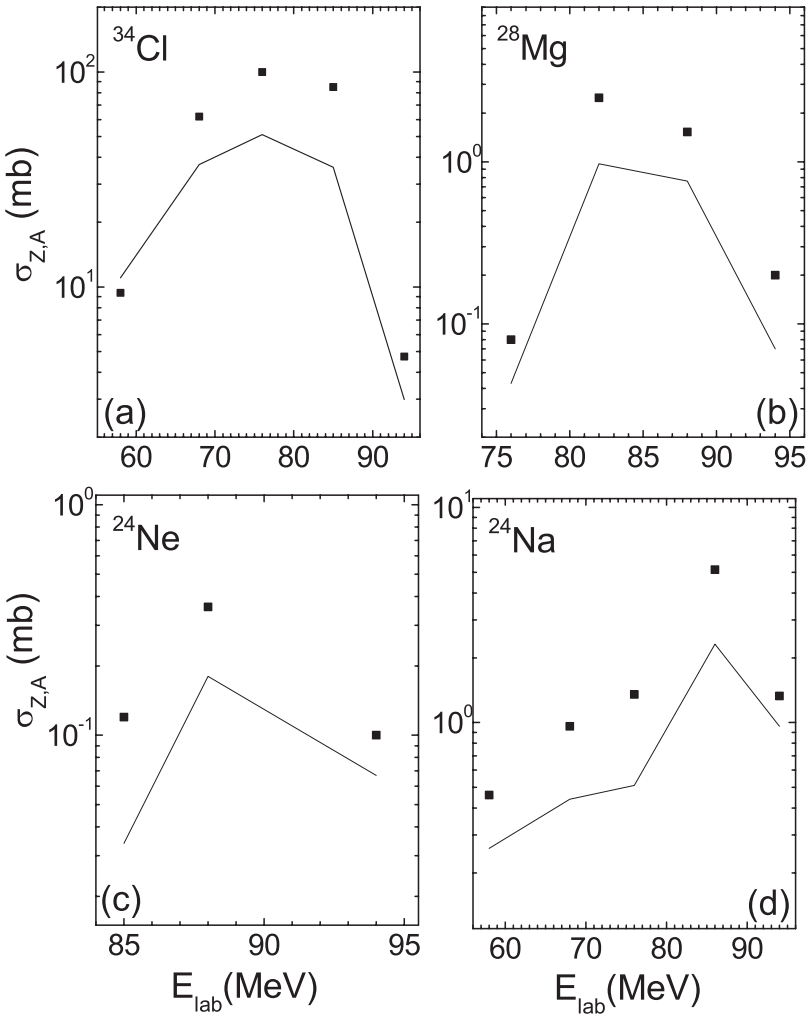

FIG. 5. Calculated (solid lines) and experimental (solid squares) [28] yields of the indicated nuclei in the ^{16}O+^{27}Al reaction as a function of bombarding energy.

a two-body configuration is kept along the trajectory, is the quasifission phenomenon.

The emission probability $W_{Z,A}(E^*_{\rm CN}, J)$ of a fragment (Z,A) is calculated as the product of the DNS formation probability and the DNS decay probability:

$$W_{Z,A}(E^*_{\rm CN}, J) = \frac{P_{Z,A} P^R_{Z,A}}{\sum_{Z',A'} P_{Z',A'} P^R_{Z',A'}}, \qquad (2)$$

where the indexes Z' and A' go over all possible channels from neutron evaporation to the symmetric splitting. The probability $P_{Z,A}$ is the equilibrium limit of the master equation (see [19] for details) given by

$$P_{Z,A}(E^*_{\rm CN}, J) \sim \exp[-U(R_m, Z, A, J)/T_{\rm CN}(J)]x. \qquad (3)$$

Here, the n-, p-, d-, and t-evaporation channels are taken into consideration with $U(R_m, Z, A, J) = 0$. The quasifission barrier B^{qf}_R, calculated as the difference between the bottom of the inner pocket and the top of the external barrier, prevents the decay of the DNS along the R-degree of freedom with the weight $P^R_{Z,A}$ given as

$$P^R_{Z,A} \sim \exp\left[-B^{qf}_R(Z, A, J)/T_{Z,A}(J)\right]. \qquad (4)$$

In Eqs. (3) and (4) $T_{\rm CN}(J)$ and $T_{Z,A}(J)$ are the temperatures of the CN and the DNS, respectively. For the emission of particles with $Z < 2$, $T_{Z,A}(J) = T_{\rm CN}(J)$ and $B^{qf}_R(Z, A, J)$ is equal to the particle binding energy plus the value of the Coulomb barrier at $Z \neq 0$. The Fermi-gas model is employed to compute the temperature, with a level-density parameter $a = 0.114A + 0.162A^{2/3}$ [19,20].

In the calculations, we use formulas (1) and (2) to treat the sequential statistical decay (the evaporation of light particles and/or the binary decay) of the hot CN and the quasifission. The generation of a whole cascade of decay channels is performed with the Monte Carlo method. We continue to trace the decay processes until all fragments become cold (i.e., when the excitation energy of fragments is smaller than its neutron emission threshold). The number n of events generated in the Monte Carlo technique was chosen according to the smallest decay probability, which is $\sim 1/n$. $n > 10^4$ iterations is large enough for obtaining the calculated results with high accuracy.

III. RESULTS OF CALCULATIONS

A. Role of N/Z ratio

We calculated the charge distribution of the ^{92}Kr+^{40}Ca reaction at bombarding energy $E_{\rm lab} = 5.5$ MeV/nucleon and compared it with the charge distribution of the neutron-deficient ^{78}Kr+^{40}Ca reaction at the same bombarding energy

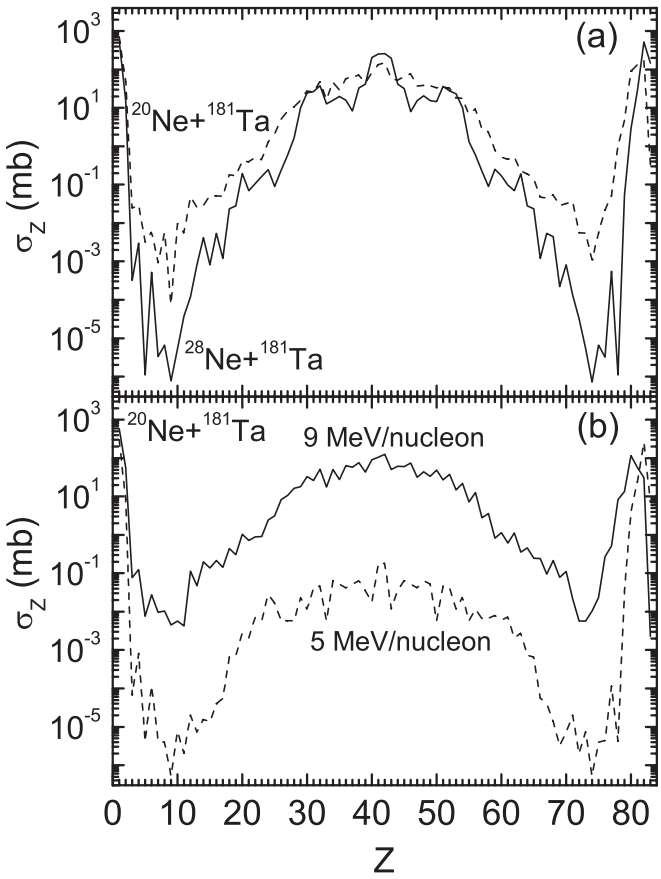

FIG. 6. (a) Calculated charge distributions of the products in the reactions ^{20}Ne+^{181}Ta (dashed line) and ^{28}Ne+^{181}Ta (solid line) at $E_{\rm lab} = 7.5$ and 4.95 MeV/nucleon, respectively. (b) Calculated charge distributions of the products in the reaction ^{20}Ne+^{181}Ta at $E_{\rm lab} = 5$ MeV/nucleon (dashed line) and 9 MeV/nucleon (solid line).

[6]. The calculated maximum angular momenta and CN excitation energies (at $J = 0$) involved in the ^{92}Kr+^{40}Ca and ^{78}Kr+^{40}Ca reactions are $J_{\rm max} = 82$, $E^*_{\rm CN} = 138$ MeV and $J_{\rm max} = 73$, $E^*_{\rm CN} = 99$ MeV, respectively. The driving potentials (normalized to the energies of the corresponding rotating CN), which are responsible for the formation of different DNS configurations, are shown in Fig. 1 for both reactions. Comparing the driving potentials for these reactions, one can conclude that the odd-even staggering decreases with increasing N/Z ratio in the system. The main reason for this is that the pairing energy decreases with increasing mass number of the nucleus. The pairing energies and shell corrections of the DNS nuclei are included in the driving potential through their binding energies. So, the staggering effects in the yields of the final products are related to the corresponding structure effects in the nuclear binding energies [25]. One can see that for the neutron-deficient system the potential energy is lower than for the neutron-rich system at the same value of angular momentum [the value of $B_1 + B_2 - B_{12}$ increases faster than $V(R_m, Z, A, J = 0)$ decreases with increasing total neutron number], which means that the formation of the DNS configurations is more probable for the neutron-deficient system. So, one can expect a larger yield of fission-like fragments in the neutron-deficient system than in the neutron-rich one. With increasing angular momentum, the potential energy for symmetric DNS configurations becomes negative at $J > J_0 = 45$ for ^{78}Kr+^{40}Ca and at $J > J_0 = 67$ for ^{92}Kr+^{40}Ca. At these large angular momenta the calculated driving potentials show a global minimum at the symmetric DNS but not at the CN configuration and the charge (mass) drift pushes the system toward symmetry. This indicates that complete fusion becomes energetically denied and higher J waves do not lead to fusion but to quasifission, resulting in the fragments produced as the binary decay products of the transient DNS originating from the target-projectile DNS. This implies that at higher partial waves, most of the heavy complex fragments are produced by quasifission. At $J \approx J_0$ the CN and symmetric DNS potential energies coincide, and we can observe the coexistence of the quasifission and fusion-decay events. Thus, at the value of J_0 the reaction mechanisms become less clear-cut. At $J < J_0$ the driving potential is positive, the CN configuration is energetically more favorable than any DNS configuration, and the decay products are mainly from the decay of the excited CN.

In Fig. 2, we compare the charge distributions of the emitted complex fragments in the reactions ^{78,92}Kr(5.5 MeV/nucleon) + ^{40}Ca. In both cases, odd-even effects are present in the production cross sections

$$\sigma_Z(E_{\rm c.m.}) = \sum_A \sigma_{Z,A}(E_{\rm c.m.}) \tag{5}$$

of fragments with $Z = 2$–12, while for heavier fragments these effects are not visible because the odd-even structures of the charge distributions are washed out due to the sequential evaporation. So, the amplitude of the staggering depends on the deposited energy. It was also found recently in Ref. [26], where the staggering depends in a more complicated way on the history of the evaporation chain than the schematic interpretation suggested in Ref. [25]. In Ref. [25] a staggering is presented in the isotopic yields at the last but one evaporation step through the pairing effect on nucleon separation energies.

In Fig. 2 the odd-even staggering is much smaller for the neutron-rich system compared to the neutron-deficient one. The maxima of the yields of symmetric fragments are located at the same position for both systems, but for the neutron-rich system the dependence on Z is flatter. The evaporation residue charge distributions are shifted to smaller Z values for the neutron-deficient system. It is interesting to see that the yields of the emitted complex fragments are much smaller in the ^{92}Kr+^{40}Ca reaction. For example, the cross section for carbon emission is about 1/6 as large as that in the ^{78}Kr+^{40}Ca reaction. This is mainly because of the smaller formation probability of corresponding DNS configurations in the ^{92}Kr+^{40}Ca reaction compared to the ^{78}Kr+^{40}Ca reaction. Note that the calculated cross sections for the ^{78}Kr+^{40}Ca reaction are in good agreement with the experimental data [6].

The mass distributions

$$\sigma_A(E_{\rm c.m.}, J) = \sum_Z \sigma_{Z,A}(E_{\rm c.m.}, J) \tag{6}$$

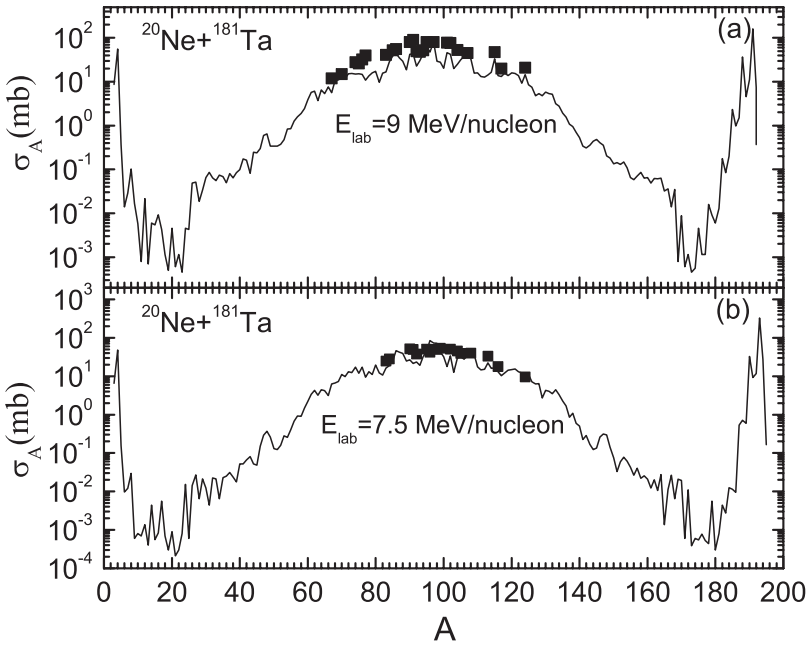

FIG. 7. Calculated (solid lines) and experimental (solid squares) [29] mass distributions of the products in the reactions ^{20}Ne+^{181}Ta at $E_{\rm lab}$ = (a) 7.5 and (b) 9 MeV/nucleon.

of the reaction products and the dependence of the average total kinetic energy (TKE)

$$\langle \mathrm{TKE}\rangle(Z) = \sum_{A,J=0}^{J_{\max}} \left[V(R_b, Z, A, J=0) + \frac{\hbar^2 f J(fJ+1)}{2\mu R_b^2} \right] \times \frac{\sigma_{Z,A}(E_{\mathrm{c.m.}}, J)}{\sigma_Z(E_{\mathrm{c.m.}})}, \qquad f = \frac{0.85\mu R_m^2}{\Im(R_m, A, \beta_1, \beta_2)}, \tag{7}$$

of the decay products versus the charge number Z are predicted in Figs. 2(b) and 3 for the reactions ^{92}Kr(5.5 MeV/nucleon) + ^{40}Ca and ^{78}Kr(5.5 MeV/nucleon) + ^{40}Ca In Eq. (7), $\Im$ is the moment of inertia of the DNS calculated in the sticking limit [19]. For the neutron-deficient and neutron-rich systems, the general behaviors of mass distributions are similar to those of charge distributions. The average TKE follows the value of the corresponding Coulomb barrier and grows globally with Z. At fixed Z and angular momentum, and similar quadrupole deformation parameters of the fragments, the height of the Coulomb barrier for the neutron-deficient system is larger than the one for the neutron-rich system. The calculated TKE for the ^{78}Kr+^{40}Ca reaction is in a good agreement with the experimental data [27].

For the ^{16}O(5.9 MeV/nucleon) + ^{27}Al and ^{22}O(2.95 MeV/nucleon) + ^{27}Al reactions, $J_{\max} = J_{cr} = 36$, $J_0 = 15$ and $J_{\max} = J_{\rm kin} = 30$, $J_0 = 28$, respectively, and the excitation energies of the CN ^{43,49}Sc formed are almost the same, $E^*_{\rm CN}(J=0) \approx 74$ MeV. Since $J_0 < J_{\max}$ for both reactions,

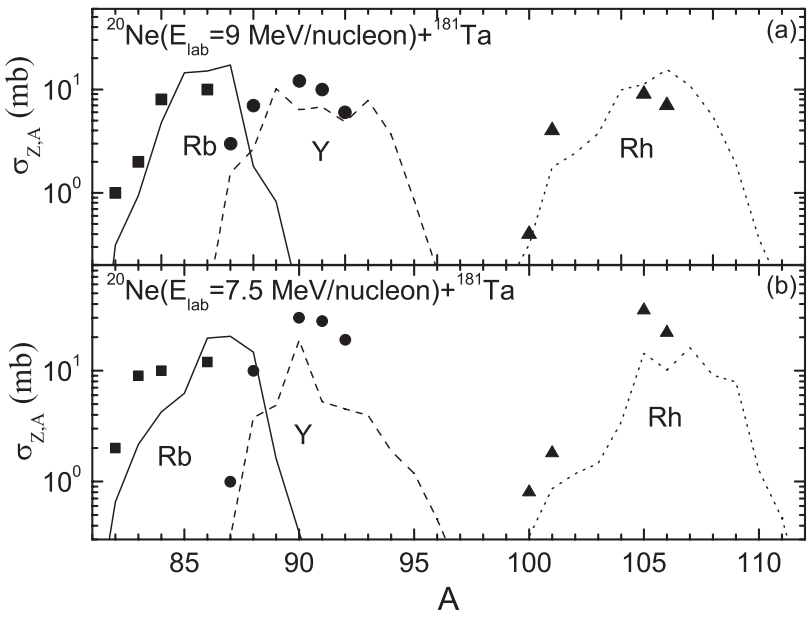

FIG. 8. Calculated (lines) and experimental (solid symbols) [29] yields of the isotopes of indicated nuclei Rb, Y, and Rh in the ^{20}Ne+^{181}Ta reaction at $E_{\rm lab}$ = (a) 7.5 and (b) 9 MeV/nucleon.

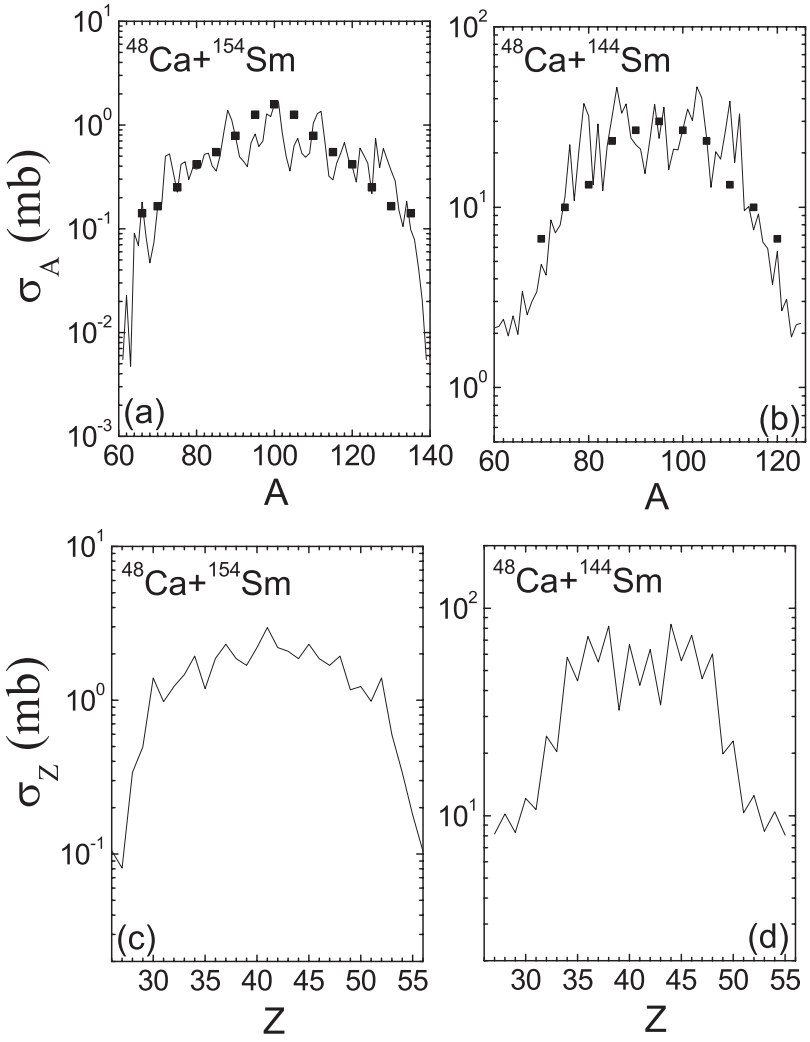

FIG. 9. Calculated (solid lines) and experimental (solid squares) [30] mass distributions and calculated (solid lines) charge distributions of the products in the reactions ^{48}Ca($E_{\rm lab}$ = 4.65 MeV/nucleon) + ^{144}Sm (right side) and ^{48}Ca($E_{\rm lab}$ = 4.2 MeV/nucleon) + ^{154}Sm (left side).

the quasifission channel dominates among other competing channels. As a result, the shapes of charge distributions at $Z < 17$ in these two reactions are rather similar [Fig. 4(a)]. However, for the neutron-deficient system, the evaporation residue charge distributions are shifted to smaller values of Z and the yields of symmetric and near-symmetric fragments are larger. As shown in Fig. 5, our method is suitable for describing the yields of the indicated nuclei ^{24}Ne, ^{24}Na, ^{28}Mg, and ^{34}Cl in the ^{16}O+^{27}Al reaction.

The dependencies of the cross section σ_Z on Z are presented in Fig. 6(a) for the reactions ^{20}Ne($E_{\rm lab}$ = 7.5 MeV/nucleon) + ^{181}Ta ($J_{\max} = J_{cr} = 63, J_{\rm kin} = 77, J_0 = 77$) and ^{28}Ne($E_{\rm lab}$ = 4.95 MeV/nucleon) + ^{181}Ta ($J_{\max} = J_{\rm kin} = 79, J_{cr} = 84, J_0 = 85$). In both cases, the CN is produced with excitation energy $E^*_{\rm CN}(J = 0) = 101$ MeV. Since $J_{\max} < J_0$ for these reactions, the same trends in the charge distributions are expected. For these heavy systems, the symmetric and near-symmetric decays considerably contribute to charge distribution even at $J_{\max} < J_0$. The reason is that the driving potentials have deep minima for corresponding symmetric and near-symmetric DNSs. Because of this the formation of nearly symmetric DNS is quite probable. For both systems, the yields of nearly symmetric fragments are comparable because for the neutron-rich system the value of $J_{\max}$ is larger by about factor of 1.3. One can see that for heavy systems the odd-even effects are much weaker than those for the light systems discussed above. Note that the calculated and experimental [29] mass distributions of the products (Fig. 7) and yields of the isotopes of nuclei Rb, Y, and Rh (Fig. 8) of the ^{20}Ne+^{181}Ta reaction at bombarding energies 7.5 and 9.0 MeV/nucleon are in good agreement.

The calculated yields of products in the reactions ^{48}Ca($E_{\rm lab}$ = 4.65 MeV/nucleon) + ^{144}Sm[$J_{\max} = J_{\rm kin} = 80$, $J_{cr} = 85$, $J_0 = 70$, $E^*_{\rm CN}(J = 0) = 63.8$ MeV] and ^{48}Ca($E_{\rm lab}$ = 4.2 MeV/nucleon) + ^{154}Sm[$J_{\max} = J_{\rm kin} = 63$, $J_{cr} = 92$, $J_0 = 89$, $E^*_{\rm CN}(J = 0) = 63$ MeV] are compared with available experimental data [30] in Fig. 9. The maximum yield of the fragments occurs at nearly symmetric fragmentations where the DNS potential energy has a deep minimum. The calculated mass distributions have more oscillations than the measured ones because the inaccuracy of the mass measurements smoothes the experimental distributions. By taking into consideration the experimental uncertainties in the measurement of mass, the agreement between the calculated and experimental data [30] is quite good. Since $J_{\max}(^{48}\text{Ca}+^{144}\text{Sm}) > J_{\max}(^{48}\text{Ca}+^{154}\text{Sm})$, $J_{\max} > J_0$ in the

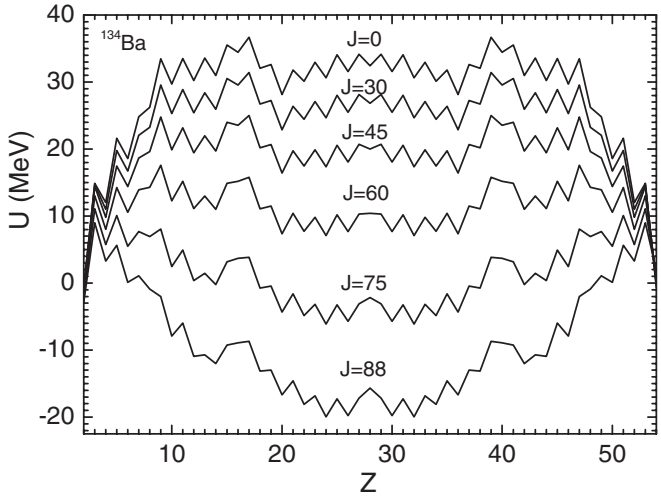

FIG. 10. The same as in Fig. 1, but for the CN ^{134}Ba at $J = 0$, 30, 45, 60, 75, and 88.

^{48}Ca+^{144}Sm system, and $J_{max} < J_0$ in the ^{48}Ca+^{154}Sm system, the yields of products in the ^{48}Ca+^{144}Sm reactions are larger by factor of about 30 than those in the ^{48}Ca+^{154}Sm reaction. The behaviors of the charge distributions are rather similar to those of the mass distributions [Fig. 9 (lower part)].

B. Role of entrance channel asymmetry

To investigate the influence of entrance channel asymmetry on the reaction mechanism and on decay properties of excited nuclear system, we studied the reactions ^{86}Kr+^{48}Ca at bombarding energy 5.5 MeV/nucleon and ^{122}Sn+^{12}C at 12 MeV/nucleon, which lead to the same CN ^{134}Ba with the same excitation energy $E^*_{CN} = 130$ MeV at $J = 0$. The maximal angular momenta for the capture process are $J_{max} = 88$ for the ^{86}Kr+^{48}Ca reaction and $J_{max} = 47$ for the ^{122}Sn+^{12}C reaction. The driving potentials for these reactions are presented in Fig. 10 at different angular momenta. One can see that $J_0 \approx 70$ for these systems, which means that for the ^{122}Sn+^{12}C reaction ($J_{max} < J_0$) the fission-like fragments are formed with smaller probability compared to the ^{86}Kr+^{48}Ca reaction ($J_{max} > J_0$). In Fig. 11 we present the charge distributions of decay fragments in these reactions. As expected, the fission-like fragments have much smaller yields in the ^{122}Sn+^{12}C reaction. The complex fragment emission cross sections are higher in the ^{86}Kr+^{48}Ca reaction. For the ^{86}Kr+^{48}Ca reaction, the potential energy becomes negative at $J = J_0 \approx 70$, which means that the symmetric DNS configurations become energetically favored and most of the fission-like fragments originate from the quasifission process in this reaction.

Thus, at fixed bombarding energy different entrance channel asymmetries lead to different maximum angular momenta J_{max}. If $J_{max} > J_0$ ($J_{max} < J_0$) the quasifission (the complete fusion) mainly contributes to the charge distribution. Different reaction mechanisms result in different shapes of charge distribution.

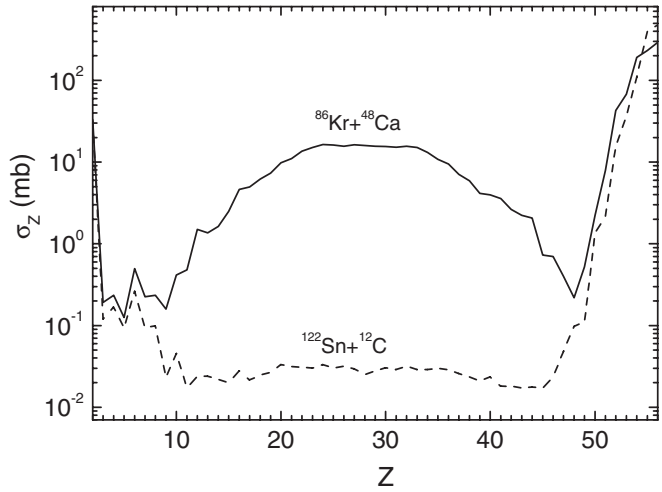

FIG. 11. Calculated charge distributions of the products in the reactions ^{86}Kr+^{48}Ca (solid line) at $E_{lab} = 5.5$ MeV/nucleon and ^{122}Sn+^{12}C (dashed line) at $E_{lab} = 12.0$ MeV/nucleon.

C. Influence of the deposited energy

The calculated charge distributions for the ^{16}O+^{27}Al reaction at $E_{lab} = 4.77$ MeV/nucleon [$E^*_{CN}(J = 0) = 62$ MeV, $J_{max} = J_{kin} = 31$, $J_{cr} = 36$] and $E_{lab} = 2$ MeV/nucleon [$E^*_{CN}(J = 0) = 34$ MeV, $J_{max} = J_{kin} = 12$, $J_{cr} = 36$] are shown in Fig. 4(b). Since for both bombarding energies, the values of J_{max} are different and $J_0 = 15$, the charge distribution strongly depends on E_{lab}. In the ^{16}O($E_{lab} = 2$ MeV/nucleon) + ^{27}Al reaction, $J_{max} < J_0$, the quasifission is suppressed, and the charge distribution is typical for the complex emission from the excited CN. In contrast to the ^{16}O+^{27}Al reaction, for the ^{20}Ne+^{181}Ta reaction at $E_{lab} = 9$ MeV/nucleon [$E^*_{CN}(J = 0) = 128$ MeV, $J_{max} = J_{cr} = 63$] and $E_{lab} = 5$ MeV/nucleon [$E^*_{CN}(J = 0) = 56$ MeV, $J_{max} = J_{kin} = 26$, $J_{max} < J_0 = 77$] the charge distributions are rather similar [Fig. 6(b)]. The yields of products increase and the staggering effects are washed out with increasing E_{lab}.

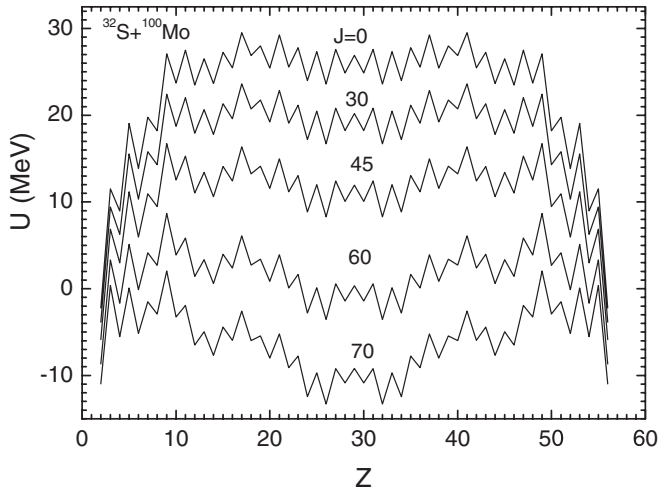

FIG. 12. The same as in Fig. 1, but for the ^{32}S+^{100}Mo reaction at $J = 0$, 30, 45, 60, and 70.

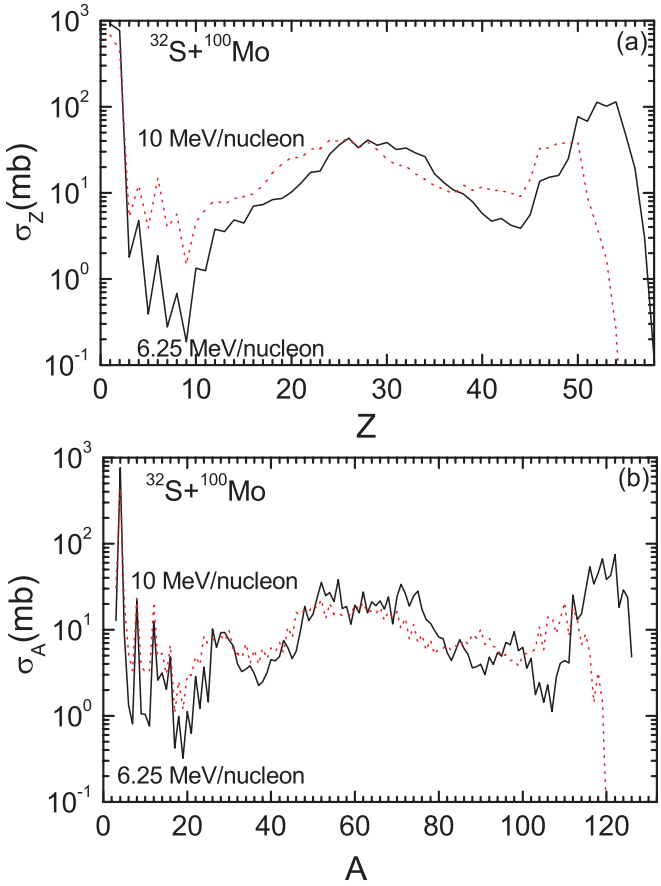

FIG. 13. (Color online) Calculated (a) charge and (b) mass distributions of the products in the ^{32}S+^{100}Mo reaction at $E_{\rm lab}$ = 6.25 MeV/nucleon (solid line) and $E_{\rm lab}$ = 10.0 MeV/nucleon (dashed line).

We study also an evolution of charge and mass distributions of the products with increasing deposited energy in the reaction ^{32}S+^{100}Mo. At bombarding energies 6.25 and 10 MeV/nucleon the maximum angular momentum for the capture process is $J_{\rm max}$ = 71 and the excitation energies of CN are $E^*_{\rm CN}$ = 122 and 212 MeV, respectively. Driving potentials for this system are presented in Fig. 12, where one can see that $J_0 \approx 60$. The expected charge distributions of the products are presented in Fig. 13. As seen, the maxima for fission-like fragments and evaporation residues are shifted to lower Z at higher excitation energies. Production cross sections of complex fragments increase by a factor of about 8 with increasing bombarding energy from 6.25 to 10 MeV/nucleon. The predictions of the mass distributions for this reaction at bombarding energies of 6.25 and 10 MeV/nucleon are shown in Fig. 13(b).

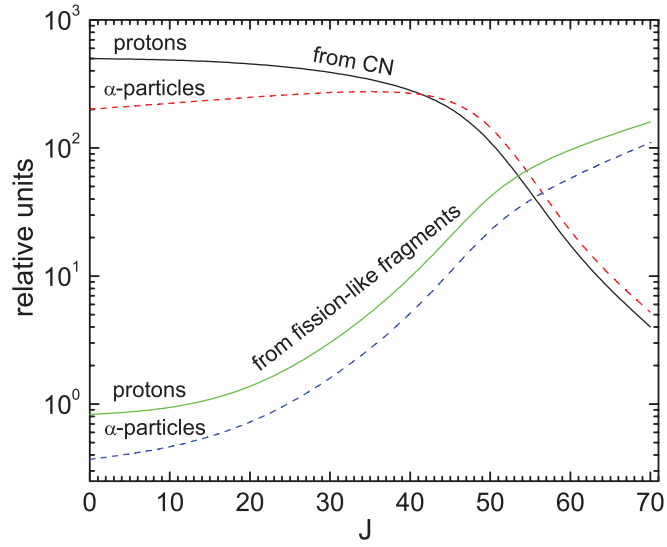

FIG. 14. (Color online) Angular momentum dependence of proton (solid line) and α-particle (dashed line) multiplicities from the CN and fission-like fragments for the ^{32}S+^{100}Mo reaction at $E_{\rm lab}$ = 6.25 MeV/nucleon.

In Table I, we compare the calculated light, charged-particle multiplicities and production evaporation residues and fission-like fragments cross sections in the reaction ^{32}S(6.25 MeV/nucleon) + ^{100}Mo with corresponding experimental data from Ref. [31]. One can see that the calculated multiplicities from the fission-like fragments are 3–4 times higher than the experimental data, while the multiplicities from the CN agree well with the experimental data. Since the multiplicity is related to the corresponding production cross section and the calculated production cross section of fission-like fragments is larger by a factor of 2 than the experimental one, we overestimate multiplicities from the fission-like fragments. So, additional theoretical and experimental studies of the multiplicities are required to discriminate unambiguously the products resulting from different reaction mechanisms.

The angular momentum dependencies of the yields of protons and α particles from the CN and fission-like fragments are presented in Fig. 14. As seen, these dependencies are opposite and at $J > J_0$ the yields of protons and α particles from the fission-like fragments become larger.

The yields of decay fragments from the excited rotating CN ^{134}Xe are shown in Fig. 15 at different $J_{\rm max}$ = 25, 45, 65, and 85 and excitation energies $E^*_{\rm CN}$ = 100, 200, and

TABLE I. Comparisons of the calculated proton and α-particle multiplicities from the CN ($M_p^{\rm ER}$ and $M_\alpha^{\rm ER}$, respectively) and from fission-like fragments ($M_p^{\rm FF}$ and $M_\alpha^{\rm FF}$, respectively) with experimental data from Ref. [31] in the ^{32}S+^{100}Mo reaction at 6.25 MeV/nucleon. Production cross sections $\sigma_{\rm ER}$ and $\sigma_{\rm FF}$ of evaporation residues and fission-like fragments, respectively, are shown as well.

	$M_p^{\rm ER}$	$M_\alpha^{\rm ER}$	$M_p^{\rm FF}$	$M_\alpha^{\rm FF}$	$\sigma_{\rm FF}$ (mb)	$\sigma_{\rm ER}$ (mb)
Exp.	0.9 ± 0.14	0.56 ± 0.09	0.055 ± 0.007	0.038 ± 0.005	130 ± 13	828 ± 50
Calc.	0.99	0.83	0.2	0.11	298	620

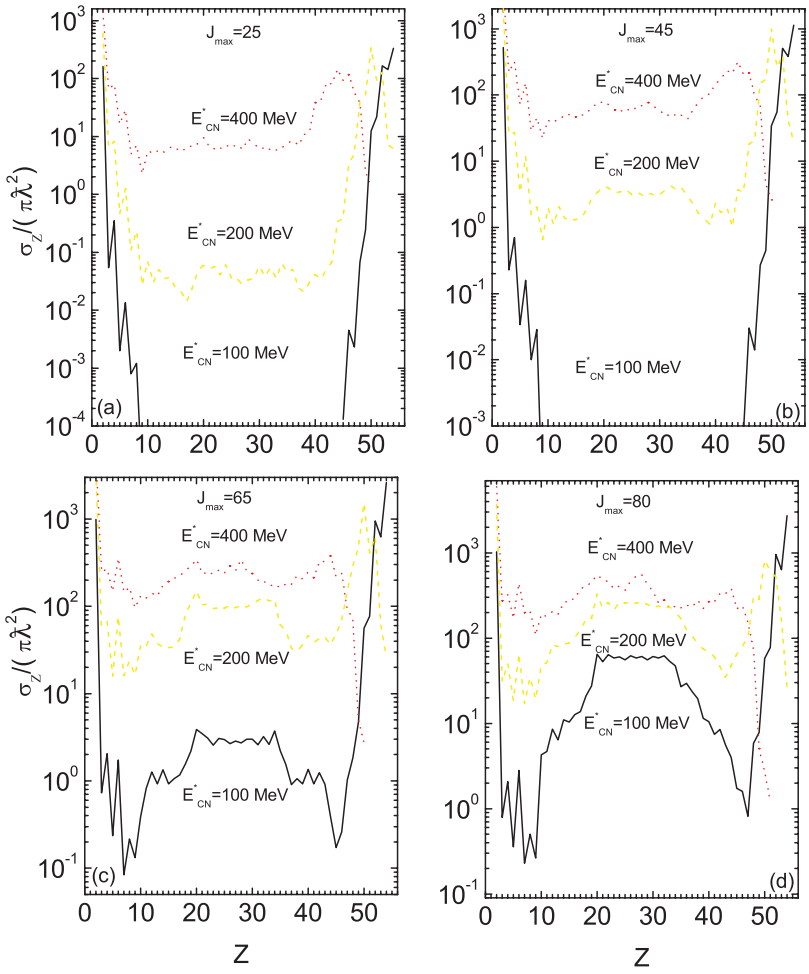

FIG. 15. (Color online) Calculated yields of the products emitted from the excited rotating ^{134}Xe nucleus at $J_{\max} = 25, 45, 65$, and 85 and $E^*_{\rm CN} = 100$ MeV (solid line), 200 MeV (dashed line), and 400 MeV (dotted line). Here, $\pi\lambda\!\!\!^{-2} = \pi\hbar^2/(\mu E_{\rm c.m.})$.

400 MeV. Here, the possibility of the CN formation with such high spins and excitation energies is not considered and it is the subject of additional studies. The yields in Fig. 15 are shown in units of $\pi\lambda\!\!\!^{-2}$ to exclude the entrance reaction channel. The driving potential for this system in Fig. 16 shows that $J_0 \approx 75$. At $E^*_{\rm CN} = 100$ and 200 MeV the shape of the distribution of charge products changes when J crosses J_0. At higher excitation energy ($E^*_{\rm CN} = 400$ MeV) this effect is not so pronounced. So, the decay of excited ^{134}Xe would depend on the reaction resulting in this CN.

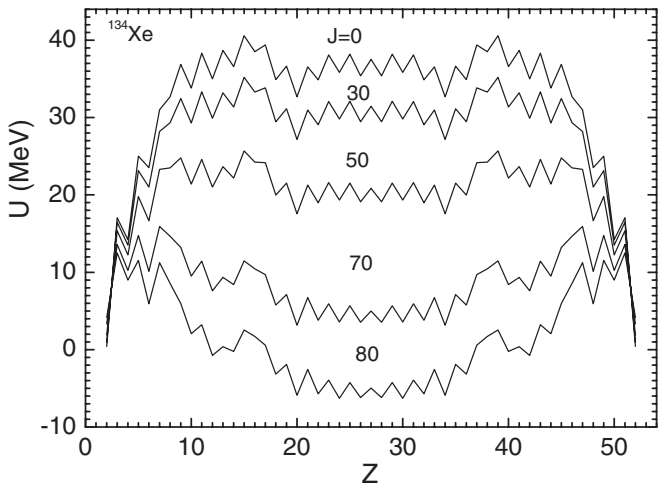

FIG. 16. The same as in Fig. 1, but for the CN ^{134}Xe at $J = 0$, 30, 50, 70, and 80.

IV. SUMMARY

The important role of entrance channel isospin, asymmetry, and bombarding energy in the emission of complex fragments was explored in the framework of the DNS model. The reaction mechanism (fusion followed by binary decay or quasifission) is mostly determined by the maximum angular momentum $J_{\max}$ deposited in the system and by the angular momentum J_0 at which the potential energy for the DNS configuration becomes smaller than the potential energy of the CN. If $J_{\max} > J_0$ or $J_{\max} < J_0$ quasifission or fusion-fission mainly contributes to the charge (mass) distribution. Different reaction mechanisms result in different shapes of charge distribution. The value of $J_{\max}$ for a capture process can be controlled by either the projectile-target mass and charge asymmetries or the kinetic energy of the projectile. The value of J_0 strongly depends on the total neutron and charge numbers of the system and, correspondingly, on the N/Z ratio and moment of inertia of the DNS. At fixed total charge number of the system, the value of

J_0 globally increases with the total neutron number. The reason is that for the neutron-rich system the potential energy and the DNS moment of inertia are larger than those for the neutron-deficient system at the same value of angular momentum, which means that J_0 is larger for the neutron-rich system.

At relatively high angular momenta, the complex fragments and the fission-like fragments in the reactions ^{92,78}Kr(5.5 MeV/nucleon) + ^{40}Ca, ^{86}Kr(5.5 MeV/nucleon) + ^{48}Ca, ^{16}O(4.77 and 5.9 MeV/nucleon) + ^{27}Al, ^{22}O(2.95 MeV/nucleon) + ^{27}Al, and ^{32}S(6.25 and 10 MeV/nucleon) + ^{100}Mo mainly originate from the quasifission process. Complete fusion followed by binary decay is dominant in the reactions ^{122}Sn(12 MeV/nucleon) + ^{12}C and ^{16}O(2 MeV/nucleon) + ^{27}Al at low angular momenta. So, different trends of the predicted charge (mass) distributions of the reaction fragments arise from different reaction mechanisms.

The shapes of charge distributions in the neutron-rich ^{92}Kr(5.5 MeV/nucleon) + ^{40}Ca and ^{22}O(2.95 MeV/nucleon) + ^{27}Al systems and the neutron-deficient ^{78}Kr(5.5 MeV/nucleon) + ^{40}Ca and ^{16}O(4.77 and 5.9 MeV/nucleon) + ^{27}Al systems are similar. However, the odd-even staggering is much smaller for the neutron-rich systems than for the neutron-deficient ones and the charge distribution near the maximum of the yield of symmetric fragments is flatter for the neutron-rich systems. The staggering effects in the yields of the final products are ruled by the corresponding structure effects in the nuclear binding energies.

For the heavy systems ^{48}Ca+^{144,154}Sm and ^{20,28}Ne+^{181}Ta, nearly symmetric decays considerably contribute to charge distribution even at $J_{\max} < J_0$. The reason is that the driving potentials have deep minima for corresponding symmetric and near-symmetric DNSs.

The yields of decay fragments from the excited rotating CN ^{134}Xe strongly depend on the maximum angular momentum deposited in the system. This dependence becomes weaker with increasing excitation energy of the CN.

ACKNOWLEDGMENTS

We thank D. Lacroix for fruitful discussions and suggestions. This work was supported by DFG and RFBR. The IN2P3-JINR, MTA-JINR, and Polish-JINR Cooperation programs are gratefully acknowledged.

[1] L. G. Moretto and G. J. Wozniak, Prog. Part. Nucl. Phys. **21**, 401 (1988).
[2] J. G. del Campo *et al.*, Phys. Rev. C **57**, R457 (1998).
[3] M. La Commara *et al.*, Nucl. Phys. A **669**, 43 (2000).
[4] J. Töke, J. Lu, and W.-U. Schröder, Phys. Rev. C **67**, 034609 (2003); B. Djerroud *et al.*, *ibid.* **64**, 034603 (2001); J. Töke, D. K. Agnihotri, W. Skulski, and W.-U. Schröder, *ibid.* **63**, 024604 (2001).
[5] J.-P. Wieleczko *et al.*, Acta Phys. Pol. B **40**, 577 (2009); in *Proceedings of the International Conference on Nuclear Structure and Related Topics*, edited by A. I. Vdovin, V. V. Voronov, and R. V. Jolos (JINR, Dubna, 2009), p. 236.
[6] G. Ademard *et al.*, Phys. Rev. C **83**, 054619 (2011); Eur. Phys. J. WEB Conf. **17**, 10005 (2011).
[7] W. A. Friedman and W. G. Lynch, Phys. Rev. C **28**, 16 (1983).
[8] R. G. Stokstad, in *Treatise on Heavy Ion Science*, edited by D. A. Bromley (Plenum, New York, 1984), Vol. III.
[9] A. J. Cole, *Statistical Models for Nuclear Decay* (Institute of Physics, London, 2000).
[10] J. Gomez del Campo, J. L. Charvet, A. D'Onofrio, R. L. Auble, J. R. Beene, M. L. Halbert, and H. J. Kim, Phys. Rev. Lett. **61**, 290 (1988).
[11] T. Matsuse, C. Beck, R. Nouicer, and D. Mahboub, Phys. Rev. C **55**, 1380 (1997).
[12] F. Auger, B. Berthier, A. Cunsolo, A. Foti, W. Mittig, J. M. Pascaud, E. Plagnol, J. Québert, and J. P. Wieleczko, Phys. Rev. C **35**, 190 (1987).
[13] R. K. Gupta, M. Balasubramaniam, C. Mazzocchi, M. La Commara, and W. Scheid, Phys. Rev. C **65**, 024601 (2002); R. Kumar and R. K. Gupta, *ibid.* **79**, 034602 (2009).
[14] R. J. Charity *et al.*, Nucl. Phys. A **476**, 516 (1988); **483**, 371 (1988).
[15] L. G. Moretto, Nucl. Phys. A **247**, 211 (1975).
[16] A. J. Sierk, Phys. Rev. Lett. **55**, 582 (1985).
[17] K. X. Jing, L. G. Moretto, A. C. Veeck, N. Colonna, I. Lhenry, K. Tso, K. Hanold, W. Skulski, Q. Sui, and G. J. Wozniak, Nucl. Phys. A **645**, 203 (1999).
[18] J. Boger and J. M. Alexander, Phys. Rev. C **50**, 1006 (1994).
[19] Sh. A. Kalandarov, G. G. Adamian, N. V. Antonenko, and W. Scheid, Phys. Rev. C **82**, 044603 (2010).
[20] Sh. A. Kalandarov, G. G. Adamian, N. V. Antonenko, and W. Scheid, Phys. Rev. C **83**, 054611 (2011).
[21] J. P. Bondorf, A. S. Botvina, A. S. Iljinov, I. N. Mishustin, and K. Sneppen, Phys. Rep. **257**, 133 (1995).
[22] V. Baran, M. Colonna, V. Greco, and M. Di Toro, Phys. Rep. **410**, 335 (2005).
[23] V. V. Volkov, Izv. AN SSSR Ser. Fiz. **50**, 1879 (1986); G. G. Adamian, A. K. Nasirov, N. V. Antonenko, and R. V. Jolos, Phys. Part. Nucl. **25**, 583 (1994); G. G. Adamian, N. V. Antonenko, and W. Scheid, Nucl. Phys. A **618**, 176 (1997); G. G. Adamian, N. V. Antonenko, W. Scheid, and V. V. Volkov, *ibid.* **627**, 361 (1997); **633**, 409 (1998); G. G. Adamian, N. V. Antonenko, and W. Scheid, Phys. Rev. C **68**, 034601 (2003).
[24] V. V. Sargsyan, G. G. Adamian, N. V. Antonenko, and W. Scheid, Eur. Phys. J. A **45**, 125 (2010); V. V. Sargsyan, G. G. Adamian, N. V. Antonenko, W. Scheid, and H. Q. Zhang, *ibid.* **47**, 38 (2011); J. Phys.: Conf. Ser. **282**, 012001 (2011); Eur. Phys. J. WEB Conf. **17**, 04003 (2011).
[25] M. V. Ricciardi, A. V. Ignatyuk, A. Kelic, P. Napolitani, F. Rejmund, K.-H. Schmidt, and O. Yordanov, Nucl. Phys. A **733**, 299 (2004).
[26] M. D'Agostino *et al.*, Nucl. Phys. A **861**, 47 (2011).
[27] J.-P. Wieleczko *et al.* (private communication).
[28] M. K. Sharma, Unnati, D. P. Singh, P. P. Singh, B. P. Singh, R. Prasad, and H. D. Bhardwaj, Phys. Rev. C **75**, 064608 (2007).
[29] R. Tripathi, K. Sudarshan, A. Goswami, R. Guin, and A. V. R. Reddy, Phys. Rev. C **74**, 014610 (2006).
[30] G. N. Knyazheva *et al.*, Phys. Rev. C **75**, 064602 (2007).
[31] E. Vardaci *et al.*, Eur. Phys. J. A **43**, 127 (2010); J. Phys.: Conf. Ser. **282**, 012012 (2011).